Surface Science 605 (2011) 1685–1693

Contents lists available at ScienceDirect

Surface Science

journal homepage: www.elsevier.com/ locate/susc

Structural analysis of PTCDA monolayers on epitaxial graphene with ultra-high vacuum scanning tunneling microscopy and high-resolution X-ray reflectivity

Jonathan D. Emery [a,1,2,3], Qing Hua Wang [a,1,2,3], Marie Zarrouati [b,3], Paul Fenter [c,2], Mark C. Hersam [a,d,*,2], Michael J. Bedzyk [a,2]

[a] Department of Materials Science and Engineering and Materials Research Science and Engineering Center, Northwestern University, 2220 Campus Drive, Evanston, IL 60208, United States
[b] École Supérieure de Physique et de Chimie Industrielles de la ville de Paris, ParisTech, 10, rue Vauquelin, 75231, Paris, France
[c] Chemical Science and Engineering Division, Argonne National Laboratory, 9700S. Cass Avenue, Argonne, IL, 60208, United States
[d] Department of Chemistry, Northwestern University, 2145 Sheridan Road, Evanston, IL 60208, United States

ARTICLE INFO

Article history:
Received 19 August 2010
Accepted 16 November 2010
Available online 24 November 2010

Keywords:
XRR
STM
PTCDA
Epitaxial graphene
Silicon carbide

ABSTRACT

Epitaxial graphene, grown by thermal decomposition of the SiC (0001) surface, is a promising material for future applications due to its unique and superlative electronic properties. However, the innate chemical passivity of graphene presents challenges for integration with other materials for device applications. Here, we present structural characterization of epitaxial graphene functionalized by the organic semiconductor perylene-3,4,9,10-tetracarboxylic dianhydride (PTCDA). A combination of ultra-high vacuum scanning tunneling microscopy (STM) and high-resolution X-ray reflectivity (XRR) is used to extract lateral and vertical structures of 0, 1, and 2 monolayer (ML) PTCDA on epitaxial graphene. Both Fienup-based phase-retrieval algorithms and model-based least-squares analyses of the XRR data are used to extract an electron density profile that is interpreted in terms of a stacking sequence of molecular layers with specific interlayer spacings. Features in the STM and XRR analysis indicate long-range molecular ordering and weak π–π* interactions binding PTCDA molecules to the graphene surface. The high degree of both lateral and vertical ordering of the self-assembled film demonstrates PTCDA functionalization as a viable route for templating graphene for the growth and deposition of additional materials required for next-generation electronics and sensors.
© 2010 Elsevier B.V. All rights reserved.

1. Introduction

Graphene is a single sheet of sp^2-bonded carbon that has tremendous potential for next-generation electronic devices due to its unique physical properties [1–6]. A promising route for achieving graphene-based electronics is the epitaxial growth of graphene on silicon carbide (SiC) (0001) surfaces via thermal decomposition. This process results in graphene formation over wafer-scale areas and enables device fabrication using conventional lithographic techniques [7]. The chemical functionalization of graphene has recently emerged as an important area in graphene research because the integration of graphene in devices and applications requires interfacing graphene with other materials while controlling its band gap and doping [8,9]. Numerous covalent and non-covalent functionalization schemes have been demonstrated on graphene surfaces [8–12]. Recently, interest in self-assembled organic monolayers of perylene-3,4,9,10-tetracarboxylic dianhydride (PTCDA) on graphene has been explored in order to introduce reactive seeding-sites for improved atomic-layer deposition (ALD) of dielectric films [13–16]. PTCDA monolayers exhibit highly ordered growth on a variety of substrates including various metals and reactive surfaces [17–22] and have been extensively studied with a number of techniques including scanning tunneling microscopy (STM) [14,20,23,24], X-ray diffraction (XRD) [24–26], and X-ray standing wave (XSW) [27–30]. In particular, STM probes the lateral structure of PTCDA layers with molecular resolution, while X-ray techniques resolve the vertical structure and allow for characterization of the substrate under the molecular layers. Previous ultra-high vacuum (UHV) STM work has shown that PTCDA forms a well-ordered monolayer on epitaxial graphene on SiC(0001) that is chemically stable and electronically decoupled from the graphene substrate [14].

Herein, we employ a combination of UHV STM and high-resolution X-ray reflectivity (XRR) to characterize PTCDA monolayers on epitaxial graphene on SiC(0001). We derive an atomic-scale structural description of functionalized epitaxial graphene formed on 6H-SiC (0001) substrates through the growth of nominally 1 or 2 monolayer (ML) thick PTCDA thin films, a model of which is shown in Fig. 1. We used high-resolution XRR [31,32] in conjunction with room-temperature UHV STM to obtain the vertical and lateral structure of

* Corresponding author. 2220 Campus Dr., Evanston, IL, 60208, United States. Tel.: +1 847 491 2696; fax: +1 847 491 7820.
E-mail address: m-hersam@northwestern.edu (M.C. Hersam).
[1] Contributed equally to this publication.
[2] Conceived the experiments and co-wrote the manuscript.
[3] Performed the experiments and analyzed the data.

0039-6028/$ – see front matter © 2010 Elsevier B.V. All rights reserved.
doi:10.1016/j.susc.2010.11.008

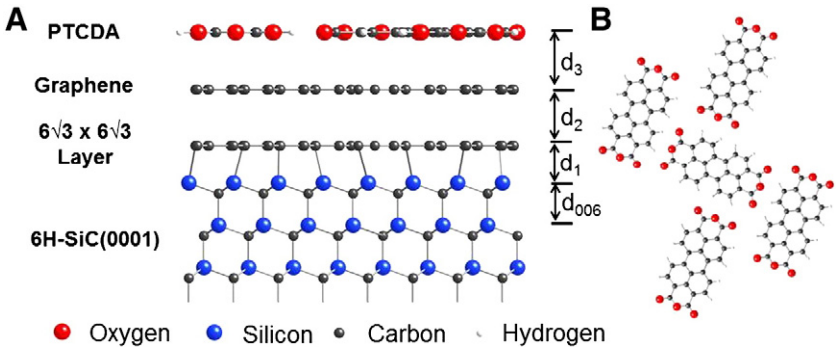

Fig. 1. (A) An idealized depiction of a 1 ML PTCDA/1 ML graphene/6H-SiC(0001) heterostructure with oxygen, silicon, carbon, and hydrogen atoms shown in red, blue, gray, and white, respectively. The crystallographic view corresponds to the [1000] projection of 6H-SiC. The $(6\sqrt{3}\times6\sqrt{3})$R30° interface is represented by the closely bonded, dense carbon atomic layer above the Si-terminated SiC bilayer. Nominally, $d_{006}=2.51$ Å, $d_1=2.30$ Å, $d_2=3.35$ Å, and $d_1=3.22$ Å. (B) Schematic of the lateral organization of the PTCDA molecules in a herringbone arrangement.

PTCDA layers on epitaxial graphene. We use a combination of Fienup-based phase-retrieval methods [33,34] and model-based least-squares analyses to derive structures describing the graphene/SiC interface and the PTCDA overlayers. The XRR and STM data show that PTCDA possesses long-range molecular ordering within the surface plane, indicating π–π* interactions between the PTCDA molecules and graphene surface. While previous XRR studies have been conducted on the basic structure of epitaxial graphene and the interface between the SiC lattice and graphene overlayers [35,36], here we use XRR to resolve the interfacial structure of the PTCDA layers on epitaxial graphene on the 6H-SiC(0001) surface. The flexibility of surface X-ray scattering allows it to be applied non-destructively in a variety of sample environments to investigate structures of buried interfaces and/or exposed surfaces.

2. Materials and methods

2.1. Sample preparation

Growth of epitaxial graphene and PTCDA monolayers were performed in a home-built UHV system with base pressures of 5×10^{-11} Torr and separate chambers for sample preparation and

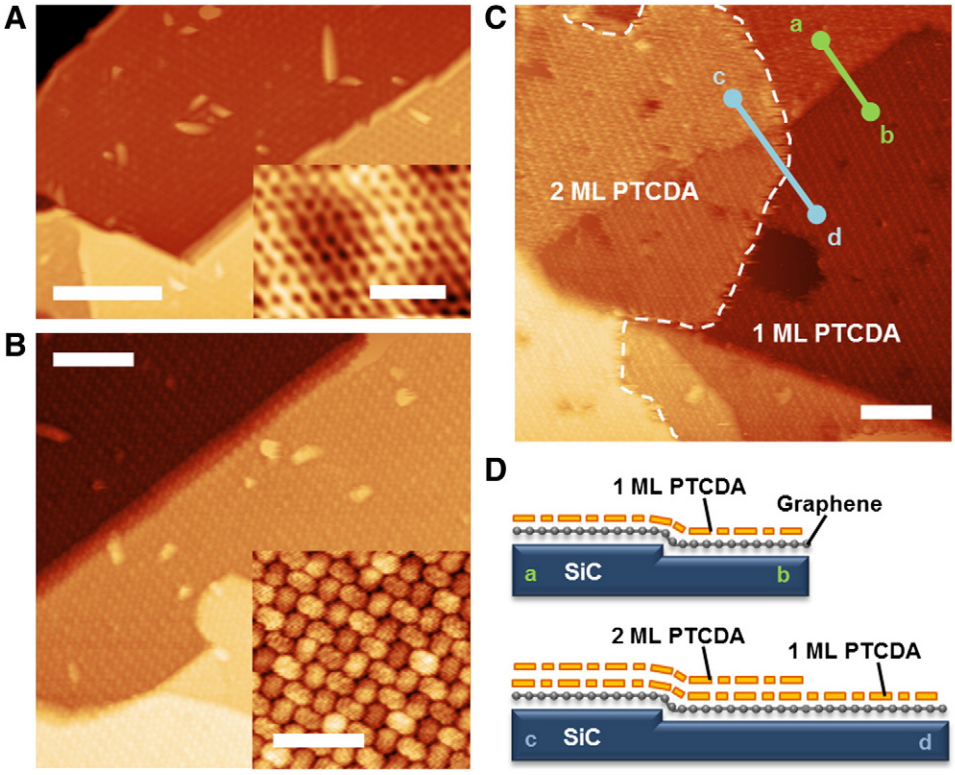

Fig. 2. UHV STM images of the sample surfaces. (A) Clean epitaxial graphene (Sample bias −2.1 V, tunneling current 50 pA, scale bar 20 nm). Inset: atomically resolved image showing the honeycomb lattice of graphene (−0.4 V, 50 pA, 1 nm). (B) Single monolayer coverage of PTCDA on epitaxial graphene (−1.9 V, 22 pA, 10 nm). Inset: Molecularly resolved image showing that the PTCDA monolayer has a herringbone arrangement (−2.0 V, 70 pA, 4 nm). (C) At ~1.5 ML PTCDA coverage, the sample concurrently possesses regions with 1 ML and 2 ML PTCDA (−1.9 V, 22 pA, 10 nm). The region to the left of the white dashed line has two layers of PTCDA, while the region to the right has one layer. (D) Schematic depth profiles of the two lines, a–b and c–d, indicated in (C). The SiC step edge in both profiles is the same, but is covered by one layer of PTCDA in line a–b and two layers in line c–d.

STM imaging. The sample preparation procedures are similar to those reported previously [14,37]. The samples were prepared using nitrogen-doped (n-type) 6H-SiC(0001) wafers (Cree, Inc.). The wafers were diced into 9 mm × 6 mm samples and cleaned by ultrasonication in acetone and isopropanol. After introduction into the UHV chamber, the samples were outgassed at 600 °C for 8–12 h. The samples were then cleaned by annealing at 1100 °C to remove the native oxide, and then graphitized by repeated heating to 1350 °C to produce a mixture of single-layer and bilayer graphene, as verified by STM imaging as shown in Fig. 2A. The PTCDA powder (97% purity, Sigma Aldrich) was loaded into an alumina-coated W crucible and thoroughly outgassed in UHV before use. The PTCDA was thermally evaporated onto the room temperature epitaxial graphene substrate, with the coverage level calibrated by subsequent STM imaging. Typical deposition rates were 0.05 ML/s. PTCDA coverage on the graphene samples was controlled by the duration of exposure to the evaporated PTCDA flux. Three samples were studied: a bare graphene sample and two PTCDA-functionalized samples with nominal coverage of 1 and 2 ML of PTCDA (see Fig. 2). Despite results indicating less than full ML coverage, these three samples are referred to in the text as the "0 ML PTCDA", "1 ML PTCDA", and "2 ML PTCDA" samples, respectively.

2.2. STM

Scanning tunneling microscopy characterization of the bare and PTCDA-functionalized graphene samples was performed in the same home-built UHV system that was used for sample preparation [38]. The system is equipped with a scanning tunneling microscope in a separate UHV chamber so that the samples could be imaged immediately after preparation without breaking vacuum. STM imaging was conducted at room temperature in constant current mode using electrochemically etched W probes. The imaging bias voltage was applied to the sample with respect to the STM tip that was grounded through a current preamplifier. Additionally, the robustness of the graphene structure was verified to be unaltered by PTCDA deposition by heating the substrate to desorb the PTCDA and then re-imaging the pristine graphene.

2.3. X-ray reflectivity

Specular XRR was measured at beamline 33-BM-C of the X-ray Operation and Research Division, Advanced Photon Source (APS), Argonne National Laboratory. The incident beam size was 0.1 mm (vertical) by 2.0 mm (horizontal). The beam was vertically focused by Pd-coated mirrors and conditioned by a double-crystal Si(111) monochromator with horizontal sagittal focusing to produce 17.00 keV X-rays with an incident flux of ~10^{10} photons/s. All samples were contained within a small beryllium dome vacuum chamber mounted directly onto the diffractometer and maintained at ~10^{-3} Torr. Reflectivity data, which can be seen in Fig. 3, is presented as a function of the momentum transfer vector with modulus, $q = 4\pi \sin(2\theta/2)/\lambda$, where 2θ is the scattering angle, and λ is the X-ray wavelength. The XRR data is also plotted as a function of the 6H-SiC reciprocal lattice unit (r.l.u.), $L = qc_{SiC}/2\pi$. Here, $c_{SiC} = 15.120$ Å [39] is the c-axis lattice constant for the 6H-SiC hexagonal unit cell. (see Fig. 1A for a side view depiction of the top three SiC bilayers.) The data points in Fig. 3A near the sharp quasi-forbidden SiC(00 L) Bragg peaks [39] $L = n$ (except $L = 6n$), where n is an integer, were removed for simplification of the reflectivity analysis.

The X-ray scattered intensity pattern in the vicinity of the specular condition was collected either by a 2D area detector or by using "rocking curves" with a point detector. A schematic comparing the two methods is shown in the Supplementary Information (Fig. S1). The majority of data ($q = 1.0$ to 6.0 Å^{-1}) were acquired using a charge-coupled device (CCD) 2D detector. This is the preferred approach because the CCD samples the rocking curve at each value in

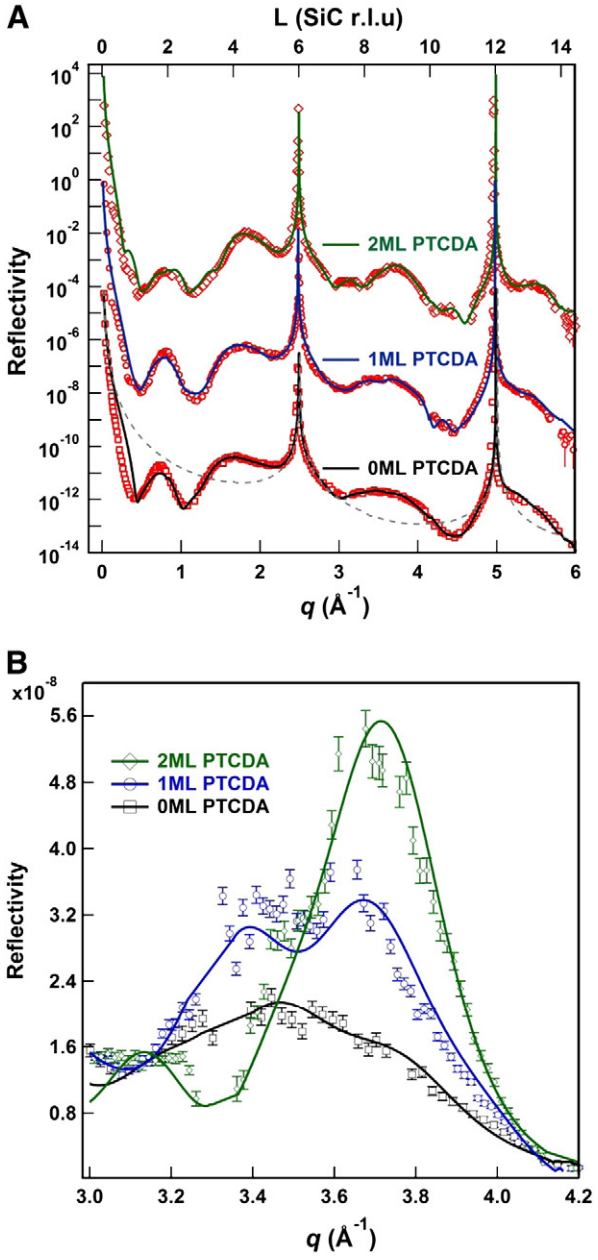

Fig. 3. X-ray reflectivity (XRR) data. (A) XRR data and fits from 0 ML PTCDA (red squares and black line), 1 ML PTCDA (red circles and blue line) and 2 ML PTCDA (red diamonds and green line). For purposes of clarity, the reflectivity signals are vertically scaled by 10^{-4}, 1, and 10^{4}, for the 0, 1 and 2 ML PTCDA samples, respectively. The calculated reflectivity for an ideally terminated 6H-SiC(0001) surface is shown for comparison as a gray dashed line along with the 0 ML data (scaled by 10^{-4}). Complete observations and interpretations of the data and fits are included in the Results and Discussion sections. (B) The same XRR data and fits as shown in (A) but on a linear vertical scale and over a limited q-range that includes the 2nd-order diffraction peak for the PTCDA/graphene thin film. Here, the data have marker symbols that match those in (A), but are colored to correspond to the matching fits for clarity.

q with a 2D detector, increasing the speed of data collection by 30 to 40 times when compared to the conventional rocking-curve method [40]. However, low-angle reflectivity data ($q = 0$ to 1.25 Å^{-1}) were acquired with a scintillation detector by performing a "rocking-curve" measurement because the lateral broadening of the specular rod due to the finite surface domain size made it difficult to fully integrate the reflectivity signal when the low-q scattering signal from the sample extended outside the CCD field of view. Broader sweeps through reciprocal space were possible with the scintillation point detector setup. CCD and point-detector data were matched to a shared range

$q = 1.0$ to $1.25\ \text{Å}^{-1}$ and combined to produce a single reflectivity curve.

The XRR signal from the CCD images were extracted following the procedure outlined in Ref. [40]. Specular and diffuse scattered intensity in the low-q range was extracted following the method described by Rauscher et al. for conformally rough surfaces [41]. Uncertainties for all data points are determined from counting statistics [40], and calculated errors in the last significant figure are provided in parentheses immediately following reported results. XRR measurements on both bare and functionalized graphene surfaces were repeated after X-ray exposure to ensure that no damage occurred as a result of X-ray radiation over the time scales necessary for data acquisition.

The specular X-ray reflectivity is defined as the ratio of the intensity of the scattered to incident X-ray intensity when the reflected angle is equal to the incident angle. The XRR is defined as [31],

$$R(q) = \left(\frac{4\pi r_e}{qA_{UC}}\right)^2 \left|(F_{UC}F_{CTR}) + F_{INT} + F_{OL}\right|^2 \quad (1)$$

where $r_e = 2.818 \times 10^{-5}$ Å is the classical electron radius and A_{UC} is the surface unit cell area. The structure factors themselves have been separated into those derived from the bulk unit cell (F_{UC}), the crystal truncation rod (CTR) form factor ($F_{CTR} = 1/(1-exp(-iqd/2))$, the interfacial structure (F_{INT}), and the overlayer (F_{OL}) contributions [32]. The F_{INT} term includes near-surface SiC bilayers which have relaxed due to graphene formation, and the F_{OL} term includes contributions from the surface reconstruction, the graphene, and the PTCDA. The structure factor for each layer is expressed as the sum over all atomic sites within a layer;

$$F(q) = \sum_m c_m f_m(q)\ exp(iqz_m)\ exp\left(-\frac{(qu_m)^2}{2}\right) \quad (2)$$

where the m^{th} atomic site has atomic scattering factor (f_m), fractional occupancy (c_m), position (z_m), and distribution width (u_m). From these parameters, a full electron density profile is constructed (see Fig. 4A). All features in the electron density profiles have been broadened by the experimental resolution of the data $\pi/q_{max} = 0.52$ Å [19].

2.4. Fienup-based analysis

It is well-known that the study of scattered X-ray intensity from a material is a powerful method to resolve surface structures; however, it is often limited by the loss of phase information in measured intensities. In the study of thin films and interfaces, this phase problem makes it challenging to directly and unambiguously relate measured specular reflectivity to an electron density profile. Recently, the use of error-correction algorithms have been expanded from applications in optics [34,42] to one-dimensional imaging of interfacial structures. The application of the Fienup algorithm to X-ray imaging, described in depth elsewhere [33], generates an electron density profile when supplied with only the known SiC crystal and a generic few-layer graphene film structure. The calculation imposes consistency between the measured diffracted intensity and the unmeasured phases by iteratively correcting the phase of the interfacial structure factor with respect to the graphene film and the substrate. In this work, the Fienup algorithm is used to derive an initial structure as a basis for later model-based analysis. Although the analysis of the interfacial structure via the Fienup-based method helps to eliminate ambiguities that might arise from assumptions in model-based fitting, full model-based fitting is necessary to achieve the most accurate results.

Fienup-based analysis was performed solely on the bare graphene sample. In this case, an 8.5 Å real-space window corresponding to the interfacial region of interest was defined. This range covers the top 3 SiC bilayers and extends to the 1st graphene layer. No structural

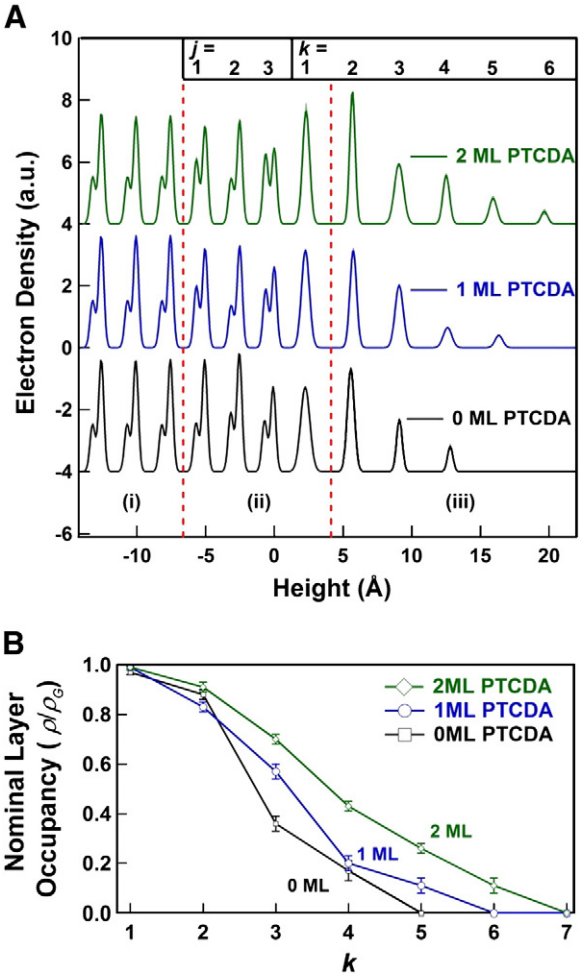

Fig. 4. (A) Extracted electron density profiles (offset vertically by −4, 0, and +4 respectively) from matching fits in Fig. 3A. Layers are identified by their subscripts, j and k. Region (i) is the bulk SiC structure that was fixed during fitting procedures. Region (ii) is the defined interface region, consisting of 3 SiC bilayers and the $(6\sqrt{3}\times6\sqrt{3})$R30° reconstructed layer ($k = 1$). Region (iii) includes both the graphene and PTCDA overlayers. The general increase in electron density in the overlayers is observable in layers $k = 2$–6 as PTCDA layers are added to the bare graphene. 1σ uncertainties in the derived electron density profiles are on the order of the line widths. (B) The fit determined occupation of each overlayer relative to the electron density in a sheet of graphene. General increases in each partially occupied layer, as well as additional growth in layers $k = 5$ and 6 are observable with 1 ML and 2 ML PTCDA deposition.

assumptions were made in the space between the top-most Si layer and the 1st graphene layer. The graphene film was assumed to consist of three layers of decreasing occupancy, and with interlayer distances set to the nominal graphite d-spacing, $d_G = 3.35$ Å, as obtained from preliminary model-based fits of the data. To ensure that the assumed height of the graphene overlayer is not dictating the interface structure, a sequence of Fienup-based analyses were run, each with the graphene film layer located at varying heights (d) above the sample. To encompass a range that may yield reasonable structures, analysis was completed from a "compressed" structure where graphene was placed at $d = 1$ Å above the top SiC bilayer, to a "stretched" interface where $d = 8$ Å. The results for the Fienup-based analysis were used in the design of the model for the least-squares fitting procedure, and are included in the Supplementary Information.

2.5. Model-based analysis

Least-squares fitting was performed by allowing structure parameters to vary while fitting models to the data. Free parameters for

the analysis include bilayer displacement of the top three ($j=1,2,3$) SiC bilayers, ($\Delta z_{BL,j}$), Si and C occupancy of the top three bilayers ($c_{Si,j}$ and $c_{C,j}$), as well as occupancy, positions, and root-mean-squared (RMS) distribution widths for the ($k=1$ to 6) overlayers ($c_{OL,k}$, $z_{OL,k}$, $u_{OL,k}$). Subscript values for each layer increase from the bulk towards the top the film layer (see Fig. 4A). For simplicity, we report all fractional occupancies in the SiC crystal with respect to the fully occupied Si (1.707 $e^-/Å^2$) or C (0.733 $e^-/Å^2$) single-crystal values (i.e., $c_{Si,1}=\rho_1/1.707\ e^-/Å^2$), and all overlayer fractional occupancies are reported with respect to a fully occupied graphene layer ($\rho_G=2.2930\ e^-/Å^2$). The PTCDA areal density is derived from analysis of the STM images of the 1 ML PTCDA surface unit cell that has 2 molecules and an area of 317.18 $Å^2$ (Fig. 2C). This corresponds to $\rho_{PTCDA}=1.26\ e^-/Å^2$ ($=24Z_C+6Z_O+8Z_H$)/158.59 $Å^2$, where Z_C, Z_O, and Z_H are the atomic numbers of carbon, oxygen, and hydrogen, respectively), giving $\rho_{PTCDA}/\rho_G=0.55$. Here, it is also important to note that in the limit where the diffuse scattering around the surface signal is fully integrated, the inherent substrate surface roughness (i.e., due to steps on the SiC lattice), which is attributed to the presence of SiC surface steps, does not affect the measured CTR intensity [43]. The use of the area detector enables us to obtain and integrate the diffuse scattering intensity from the specular rod. Consequently, the apparent roughness obtained during least-squares analysis (defined using the Robinson beta roughness formalism [32]) converged to zero.

Bare graphene (0 ML PTCDA), 1 ML PTCDA, and 2 ML PTCDA data were allowed 21, 24, and 27 free parameters, respectively. Analysis was limited to 3 graphene layers for the non-functionalized sample, with a single new atomic layer added for each layer of PTCDA. In the XRR analysis, we do not explicitly distinguish between the graphene and PTCDA layers. Since we find from STM (see Section 3.1 below) that the PTCDA covers graphene steps smoothly, this approximation is reasonable considering that the nominal interlayer spacings for graphene layers ($d_G=3.35$ Å), and for the planar PTCDA(102) layers ($d_{PTCDA}=3.22$ Å) [25], are well matched. This close match means that additional PTCDA molecules will populate graphene planes if no graphene is present, i.e., in the case of incomplete bilayer coverage. Additionally, because our vertical real-space resolution cannot discern individual features at distances less than $\pi/q_{max}=0.52$ Å, we are not able to resolve PTCDA and graphene molecules within the same layer only separated by 0.1–0.2 Å. However, we expect that the differences between graphene and PTCDA may be sensed through the precise locations and RMS widths of the PTCDA layers. Bottom-up consistency was imposed, where results from the bare graphene/SiC data were used to constrain parameters from the more complex PTCDA-functionalized systems.

3. Results

3.1. STM

The epitaxial graphene surfaces after UHV graphitization and PTCDA monolayer deposition are seen in the room temperature UHV STM images of Fig. 2. The clean epitaxial graphene surface is shown in Fig. 2A, and has a mixture of single-layer and bilayer regions. Underlying atomic steps in the SiC substrate are visible in the topography of Fig. 2A, as the graphene sheet conformally covers the substrate. The inset of Fig. 2A shows an atomically resolved STM image of the graphene honeycomb lattice. PTCDA forms a well-ordered monolayer with a herringbone arrangement after deposition onto epitaxial graphene by thermal evaporation, as shown in Fig. 2B. The PTCDA monolayer continuously covers the underlying SiC atomic steps wherever the graphene sheet also continuously covers the SiC steps, as was shown previously [14]. The PTCDA monolayer is conformal, and the existing topography of the substrate is clearly visible. As the PTCDA coverage increases, a full monolayer is formed before a second layer begins. At ~1.5 ML PTCDA in Fig. 2C, a region of 1 ML PTCDA is observed on the right half of the image and a region of 2 ML PTCDA is observed on the left half, with the boundary indicated by the dashed line. The second layer also has a herringbone arrangement with the same unit cell and is aligned with the first layer, in agreement with previous reports [44]. We also observe that both the first and second PTCDA layers continuously cover the underlying SiC steps in Fig. 2C. The depth profiles along two lines in Fig. 2C are shown schematically in Fig. 2D, and illustrate that the underlying SiC step is unchanged while the PTCDA coverage increases from one layer to two layers on the left half of Fig. 2C.

3.2. Reflectivity data

Specular reflectivity data for a bare epitaxial graphene film grown on the 6H-SiC(0001) surface are shown in Fig. 3A. The allowed bulk SiC (006) and (0012) peaks can be seen at $q=2.49\ Å^{-1}$ and $4.99\ Å^{-1}$. As a point of reference, graphite (001), (002) and (003) reflections are nominally expected at $q=1.87$, 3.74 , and $5.71\ Å^{-1}$. A broad thin-film modulation in the reflectivity is observed between $q=0.40\ Å^{-1}$ and $1.05\ Å^{-1}$with an oscillation period Δq of $0.65\ Å^{-1}$. This low-q oscillation corresponds to the relatively longer length-scale features of the electron density profile, specifically the electron-density contrast between substrate and film, indicating an approximate thin film thickness of 1 nm. As the reflectivity of the entire oscillation remains below the normalized reflectivity calculated for a truncated SiC surface (Fig. 3A), this feature indicates that the integrated average electron density of the graphene film itself is less than that of the SiC substrate [39].

The data for 1 ML and 2 ML PTCDA show a systematic trend of shifted peak positions, increased reflectivity and reduced peak width near $q=1.87\ Å^{-1}$, $3.74\ Å^{-1}$, and $5.71\ Å^{-1}$. These features are clearer when a subset of these data are shown on a linear reflectivity scale near the second-order graphene/PTCDA peak in Fig. 3B. Qualitatively, these features indicate that as PTCDA layers are added to the bare graphene surface, the film is thickening and the average d-spacing is reducing slightly. The integrated intensity is proportional to the total occupation of the layers, while the peak width is inversely proportional to the film thickness [45,46]. The data from the 2 ML PTCDA also exhibits additional thickness fringes that appear on the shoulders of the graphene peaks, indicating the coherent growth of the PTCDA film (Fig. 3A). The quality of fit for the low-q is generally poorer than the high-q, likely due to the presence of SiC surface roughness in the low-q region which causes additional diffuse scattering intensity near the specular rod in the form of Yoneda wings [47].

3.3. Model-based analysis

The best least-squares fits are shown overlaid on the data in Fig. 3. The parameters for each fit are shown in Table 1. The fits show very good agreement with data in high-q regions, indicating that the final models accurately resolve the atomic distribution of the graphene and PTCDA layers. The χ^2 and R-factors [48] were lowest with the bare graphene system and increased with system complexity. Regions of high reflectivity in which dynamical diffraction effects are dominant (i.e. $q<0.20\ Å^{-1}$, and near SiC Bragg peaks) were omitted from fits and are not reflected in the goodness-of-fit factors. When allowed to vary independently, the individual Si and C layer positions within a SiC bilayer were found to have a high degree of covariance. This issue was remedied by fixing the bilayer separation to the bulk-like value.

Consistent with previous studies, the resulting model includes changes to the near-surface SiC layers as well as the formation of a few layers of material associated with the formation of a laterally continuous graphene. As seen in Table 1 the displacements of each SiC bilayer ($\Delta z_{BL,j}$) were found to be negligible within the limits of the

Table 1
Model best-fit results.

	χ^2	R-factor	j	$\Delta z_{BL,j}$ (Å)	$c_{Si,j}$	$c_{C,j}$	k	$z_{OL,k}$ (Å)	$c_{OL,k}$	$u_{OL,k}$ (Å)
0 ML PTCDA	6.53	0.11					1	2.25(1)	0.97(1)	0.27(1)
			1	0.01(1)	0.99(1)	1.05(3)	2	5.58(2)	0.88(2)	0.17(1)
			2	0.00(1)	1.03(3)	1.24(3)	3	9.13(2)	0.36(3)	0.09(3)
			3	0.00(1)	0.75(1)	1.06(3)	4	12.80(3)	0.17(4)	0.07(6)
1 ML PTCDA	7.78	0.23					1	2.29(1)	0.99(1)	0.21(1)
			1	0.01(1)	0.90(2)	1.26(6)	2	5.77(2)	0.83(2)	0.15(1)
			2	-0.01(1)	0.95(2)	0.90(5)	3	9.09(2)	0.57(3)	0.20(3)
			3	-0.00(1)	0.75(1)	1.42(4)	4	12.61(3)	0.20(3)	0.25(5)
							5	16.32(5)	0.11(3)	0.21(9)
2 ML PTCDA	11.75	0.31					1	2.27(1)	0.99(1)	0.16(2)
							2	5.69(2)	0.91(2)	0.09(3)
			1	0.00(1)	0.89(2)	1.24(6)	3	9.07(3)	0.70(2)	0.28(3)
			2	0.01(1)	0.93(2)	1.01(5)	4	12.51(2)	0.43(2)	0.17(3)
			3	0.01(1)	0.67(2)	1.48(7)	5	15.94(4)	0.26(2)	0.21(5)
							6	19.66(6)	0.11(3)	0.2(1)

Least-squares fitting results for XRR data. Goodness-of-fit values χ^2 and R-factor are defined in Ref. [48]. Uncertainties in the last significant figure are shown in parentheses after the reported values. Indices j and k correspond to bottom-to-top SiC bilayers and nominal graphene layers, respectively. The bilayer vertical offset, Si occupancies, and C occupancies of the SiC bilayers are $\Delta z_{BL,j}$, $c_{Si,j}$, and $c_{C,j}$, respectively. The vertical position, occupancy, and RMS distribution widths of the graphene layers are $z_{OL,k}$, $c_{OL,k}$, and $u_{OL,k}$. Atomic planes corresponding to indices j and k, as well as the electron density profile corresponding to each fitting result, are shown in Fig. 4A, and relative nominal graphene coverages are shown in Fig. 4B.

error. It can also be seen that for SiC bilayers closer to the surface the Si occupancy fractions ($c_{Si,j}$) decrease and the C occupancy fractions ($c_{C,j}$) increase. The extracted electron-density profiles representing the best-fit parameters are shown in Fig. 4A. Due to the acquisition and integration of most of the diffuse scatter during the experiment, the model electron densities are found to have a beta roughness factor of zero. The electron density profiles in Fig. 4A are therefore represented with sharp interfaces devoid of surface roughness effects. Additionally, it is important to note that the electron density profiles show peaks that are combinations (Eq. (2)) of the occupancies, positions, and widths of the overlayers. For this reason, the peak heights are not directly proportional to coverage. Therefore, Fig 4B compares the total derived coverage for each layer k for the respective 0 ML, 1 ML, and 2 ML samples.

3.3.1. 0 ML PTCDA/graphene

The electron density profile for the optimized structure of the bare graphene layer is shown in Fig. 4A, with the best-fit determined parameters listed in Table 1. The first non-SiC layer ($k=1$), which is identified as the $(6\sqrt{3}\times6\sqrt{3})$R30° reconstructed layer, is positioned at a height of 2.25(1) Å above the topmost SiC bilayer, and has a nearly graphitic electron density. The three subsequent graphene layers indexed as $k=2$, 3, 4 are spaced at $\Delta z_{OL}=3.33(3)$, 3.55(4), and 3.67(4) Å , respectively. The first spacing matches well to the bulk graphite interplanar spacing, but the subsequent graphene layers show an outward relaxation.

The overall coverage (Θ) of graphene is found by adding the occupancy of the three graphene layers ($c_{OL,2-4}$). This resulting coverage of $\Theta_G=1.4(1)$ ML is reasonable considering the STM observations of domains with 1 and 2 ML graphene. We note that the XRR model fit shows that each subsequent graphene layer has an increased RMS width ($u_{OL,2}$), which is in qualitative agreement with previous X-ray, STM and theoretical results [36,49–52], although the reported values of the widths vary. An important feature of these results is their consistency with the Fienup-based direct-methods analysis [53]. For example, the occupancy of C and Si within the SiC bilayers, as well as the detailed structure of the $(6\sqrt{3}\times6\sqrt{3})$R30° reconstructed interface, agrees with the results from the Fienup-based analysis [53].

3.3.2. 1 ML PTCDA/graphene

For the optimized model of the 1 ML PTCDA system, one additional atomic overlayer ($k=5$) has been added to the 0 ML model to account for the deposited PTCDA. Referring to Fig. 3, since the positions of the broad peaks for the 1 ML PTCDA case nearly coincide with those in the 0 ML data and since STM shows smooth coverage of PTCDA over graphene steps, it is reasonable to assume that the PTCDA layers occupy nearly periodic "graphene" positions. Therefore, the electron density added by the PTCDA is represented in the model by an increased "graphene" coverage to each layer and one additional topmost layer. When compared to the 0 ML (bare graphene) results, the graphene coverage in layers $k=2$ to 5 for the 1 ML PTCDA sample rises to 1.7(1) ML, equivalent to an increase of 0.3(2) ML of graphene. Due to the difference in electron-density between graphene and PTCDA, this corresponds to 0.6(3) ML of PTCDA. The results show that PTCDA deposition grows coherently with the graphene interfacial layer over the macroscopic footprint of the X-ray beam. The results also show that layers that contain adsorbed PTCDA display increased distribution widths when compared to the bare graphene results.

3.3.3. 2 ML PTCDA/graphene

The 2 ML PTCDA results maintain the trends exhibited by the 1 ML results. The addition of the $k=6$ overlayer allows for the sufficient narrowing of the graphene peaks to provide a reasonable fit in Fig. 3A. The average d-spacing of the PTCDA/graphene layers $\Delta z_{OL,}$ now is ~3.41 Å. Note that on average, the overall interplanar spacing has decreased by 0.11 Å from 3.52 Å observed for the 0 ML PTCDA sample. This change in inter-planar spacing corresponds to a calculated shift in the thin-film reflection of $+0.13$ Å^{-1} for an idealized 2 ML PTCDA/graphene layer. This result is similar to the actual observed shift of $+0.25$ Å^{-1}, which qualitatively shows that the average d-spacing is shrinking as a result of PTCDA adsorption. The additional occupancy of the nominal graphene layers is now 1.0(2) ML, which corresponds to 1.6(3) ML of adsorbed PTCDA. This trend verifies the observations from 1 ML PTCDA case. Again, distribution widths of the atomic layers containing PTCDA are wider than those containing mostly graphene.

4. Discussion

4.1. Graphene/SiC interface structure

In order to achieve an accurate model for the PTCDA-functionalized graphene/SiC system, it is necessary to create an interface model that is consistent throughout the analysis of multiple systems. Previous research has concentrated on solving this interface structure, but a conclusion within the literature has not been unanimously reached [35,36]. Specifically, Hass et al. have performed extensive XRR studies on epitaxial graphene grown on 4H-SiC(0001) and have

proposed a model in which the interface consists of a dense carbon layer with additional carbon or silicon adatoms [36] supplying necessary additional electron density at the graphene/SiC interface. Here, we note that our attempts to fit adatom models to the data yielded reasonable fits with slightly higher χ^2 values; however, the results from the Fienup-based analysis led us to an alternate model. It is also important to note the samples from this present study differ from those of Ref. [36] in polytype, sample preparation, growth conditions, and measurement conditions, all of which could lead to differences in the interfacial structure.

Our model indicates a SiC surface with structural and stoichiometric modifications to the top three bilayers and only a single dense $(6\sqrt{3}\times6\sqrt{3})$R30° reconstructed layer at the interface. This resultant structure may be due to structural artifacts that arise during growth. Specifically, the decreased occupancies of the Si and increased occupancies of the C in the SiC bilayers deserve attention. Recent work by Ohta et al. [54] and Hupalo et al. [55], propose a growth mechanism governed by carbon diffusion at SiC step edges. This triple bilayer step-flow growth mechanism may be common in 6H-SiC due to the dominance of half unit cell terraces [56,57]. This growth mechanism would account for increased electron density as the SiC bilayers retreat, leaving a graphitic layer of carbon in the SiC planes, which would yield a higher areal electron density. While interface and growth kinetics of this system are still unclear, the increased carbon concentration at the interface is consistent with various spectroscopic studies [58,59] and is constant throughout the 0 ML, 1 ML and 2 ML PTCDA-functionalized graphene samples. As XRR is sensitive only to the electron density of a structure (with little elemental sensitivity), it is likely that more work will be required to unambiguously resolve the interface.

4.2. STM-observed lateral structure and XRR-observed vertical structure

STM imaging of PTCDA on epitaxial graphene shows the lateral structure of the organic layers with molecular resolution. The PTCDA molecules assemble into well-ordered monolayers with domains spanning hundreds of nanometers. The second PTCDA monolayer assembles on top of the first, and maintains the same herringbone arrangement and alignment with the first layer. These layers seamlessly cover both monolayer and bilayer graphene without a break in the lateral ordering. By depositing increasing amounts of PTCDA on the epitaxial graphene surface, we observe the PTCDA coverage progresses from isolated islands to a full monolayer followed by a second layer deposited on the first full monolayer. However, due to the convolution of electronic and topographic contributions to the tunneling current, we are not able to make conclusive measurements of the vertical structure of the PTCDA multilayers in STM.

XRR measurements resolve the vertical atomic-scale distribution of PTCDA overlayers on the graphene surface and supplement observations from STM. The interlayer spacing is characteristic of the nature of the bond, and surface adsorption of PTCDA is nontrivially dependent on the substrate [60]. For more reactive Cu(111) and Ag(111) surfaces, PTCDA is found to have bonding distances of 2.86 Å and 2.66 Å, respectively, indicating weak chemisorptions [27,28]. However, previous results on more inert substrates, such as Au(111), indicate physisorption [25,30]. For the PTCDA/graphene interaction, weak physisorption is expected due to the chemical inertness of graphene and the relatively large spatial extent of the π-orbitals for both the graphene and the aromatic carbon atoms in PTCDA.

Our results show that the PTCDA seamlessly coats monolayer and bilayer graphene and that the PTCDA effectively fills in partial graphene layers. Qualitatively, the increase in the intensity in the region of the graphene peaks indicates increased occupancy and thickness of the graphene layers. This observation can be seen from the 0 ML, 1 ML, and 2 ML PTCDA structures presented in Fig. 4A. This evidence supports the view that the expected π–π* stacking is occurring because the bonding distances of the PTCDA to the graphene is nearly identical to that of the graphene layers themselves. While the similarity in the bonding mechanism complicates the separation of the PTCDA and graphene structures, we can conclude that the spacing between the PTCDA and the graphene is d = ~3.40 Å. This value is very close to the sum of two van der Waals radii for aromatic molecules (here, approximated by perylene), $2r_v = 3.50$ Å. [30,61].

In addition to the interlayer spacings, XRR shows that the adsorption of the PTCDA molecules to the surface yields increased distribution widths of the upper layers from ~0.10 Å for the bare graphene to ~0.20 Å for both 1 ML and 2 ML PTCDA. There are a number of possible sources for this observation. First, as in the case of Ag(111) and Cu(111) substrates, the chemisorptive nature of the substrate-molecule interaction can cause a change in the adsorption geometries because of distortions of the carboxylic oxygen atoms [27–29,60]. However, in the case of weakly bonding systems with large intermolecular spacings, large vertical molecular distortions within a single PTCDA molecule are not expected [30]. On the other hand, it has been recently shown by *ab initio* methods that energetically favorable multilayer configurations of PTCDA have the individual molecular planes tilted from the graphene plane by a few degrees [62]. This tilt parallel to the surface could explain the observed increase in PTCDA electron density peak widths as PTCDA is deposited on the surface. Lastly, it is possible that the PTCDA is still planar and parallel to the graphene plane, but a slight mismatch in d-spacing between the PTCDA and graphene could lead to a smearing of the distribution profile.

A close relationship exists between the substrate-molecule bonding distance and the electrical properties of the system. Physisorption, characterized by large bonding distances, is an indication of the weak electronic interactions between the graphene substrate and the adsorbed PTCDA. While the results of this paper indicate a large structural separation of the PTCDA from the graphene, it does not uniquely rule out a stronger substrate-film relationship. This measurement does, however, support previous work involving scanning tunneling spectroscopy (STS) that showed that the electronic properties of the PTCDA are largely decoupled from that of the substrate in both epitaxial graphene [14] and gold substrates [21,63]. By not disrupting the outstanding electronic properties of the underlying graphene, PTCDA is thus a desirable candidate for integrating graphene with other materials, such as seeding the growth of high-*k* dielectrics in graphene-based transistors.

5. Conclusion

We have investigated the detailed structure of self-assembled PTCDA layers deposited on the epitaxial graphene/SiC(0001) surface with STM and XRR. STM shows the highly-ordered lateral structure of the PTCDA layers with molecular resolution, while the XRR results show that the PTCDA layers adsorb to the graphene surface with characteristic π–π* stacking bond lengths, thus indicating weak interaction with the graphene underlayers in agreement with evidence from STM and scanning tunneling spectroscopy studies. The complete vertical and lateral structural description of PTCDA/graphene verifies that PTCDA is well-ordered, stable, and essentially electronically decoupled from the graphene substrate. This work will thus inform future efforts to exploit organic functionalization in the design and fabrication of graphene-based devices.

Acknowledgements

This work received partial support from the National Science Foundation (Award Numbers: DMR-0520513 to the MRSEC at NU and EEC-0647560), the Office of Naval Research (Award Number N00014-09-1-0180), and the Department of Energy (Award Numbers: DE-

SC0001785, DE-AC02-06CH11357 to the CEES-EFRC, and DE-AC02-06CH11357 to the APS at ANL). In particular, the X-ray characterization and analysis by P. F. was funded by DE-AC02-06CH11357 to the CEES-EFRC. We thank Evguenia Karapetrova and Zhan Zhang of the APS XOR Sector 33 for beamline assistance.

Appendix A. Supplementary data

Supplementary data to this article can be found online at doi:10.1016/j.susc.2010.11.008.

References

[1] A.K. Geim, K.S. Novoselov, The rise of graphene, Nature Materials 6 (2007) 183–191.
[2] W.A. de Heer, C. Berger, X.S. Wu, P.N. First, E.H. Conrad, X.B. Li, T.B. Li, M. Sprinkle, J. Hass, M.L. Sadowski, M. Potemski, G. Martinez, Epitaxial graphene, Solid State Communications 143 (2007) 92–100.
[3] C. Berger, Z.M. Song, T.B. Li, X.B. Li, A.Y. Ogbazghi, R. Feng, Z.T. Dai, A.N. Marchenkov, E.H. Conrad, P.N. First, W.A. de Heer, Ultrathin epitaxial graphite: 2D electron gas properties and a route toward graphene-based nanoelectronics, The Journal of Physical Chemistry B 108 (2004) 19912–19916.
[4] K.S. Novoselov, A.K. Geim, S.V. Morozov, D. Jiang, M.I. Katsnelson, I.V. Grigorieva, S.V. Dubonos, A.A. Firsov, Two-dimensional gas of massless Dirac fermions in graphene, Nature 438 (2005) 197–200.
[5] K.S. Novoselov, A.K. Geim, S.V. Morozov, D. Jiang, Y. Zhang, S.V. Dubonos, I.V. Grigorieva, A.A. Firsov, Electric field effect in atomically thin carbon films, Science 306 (2004) 666–669.
[6] A.K. Geim, Graphene: status and prospects, Science 324 (2009) 1530–1534.
[7] Y.M. Lin, C. Dimitrakopoulos, K.A. Jenkins, D.B. Farmer, H.Y. Chiu, A. Grill, P. Avouris, 100-GHz transistors from wafer-scale epitaxial graphene, Science 327 (2010) 662.
[8] K.P. Loh, Q. Bao, P.K. Ang, J. Yang, The chemistry of graphene, Journal of Materials Chemistry 20 (2010) 2277–2289.
[9] C.N.R. Rao, A.K. Sood, K.S. Subrahmanyam, A. Govindaraj, Graphene: the new two-dimensional nanomaterial, Angewandte Chemie. International Edition 48 (2009) 7752–7777.
[10] D.C. Elias, R.R. Nair, T.M.G. Mohiuddin, S.V. Morozov, P. Blake, M.P. Halsall, A.C. Ferrari, D.W. Boukhvalov, M.I. Katsnelson, A.K. Geim, K.S. Novoselov, Control of graphene's properties by reversible hydrogenation: evidence for graphane, Science 323 (2009) 610–613.
[11] E. Bekyarova, M.E. Itkis, P. Ramesh, R.C. Haddon, Chemical approach to the realization of electronic devices in epitaxial graphene, Physica Status Solidi R 3 (2009) 184–186.
[12] D.R. Dreyer, S. Park, C.W. Bielawski, R.S. Ruoff, The chemistry of graphene oxide, Chemical Society Reviews 39 (2010) 228–240.
[13] X.R. Wang, S.M. Tabakman, H.J. Dai, Atomic layer deposition of metal oxides on pristine and functionalized graphene, Journal of the American Chemical Society 130 (2008) 8152–8153.
[14] Q.H. Wang, M.C. Hersam, Room-temperature molecular-resolution characterization of self-assembled organic monolayers on epitaxial graphene, Nature Chemistry 1 (2009) 206–211.
[15] P. Lauffer, K.V. Emtsev, R. Graupner, T. Seyller, L. Ley, Molecular and electronic structure of PTCDA on bilayer graphene on SiC(0001) studied with scanning tunneling microscopy, Physica Status Solidi B Basic Solid State Physics 245 (2008) 2064–2067.
[16] H. Huang, S. Chen, X. Gao, W. Chen, A.T.S. Wee, Structural and electronic properties of PTCDA thin films on epitaxial graphene, ACS Nano 3 (2009) 3431–3436.
[17] M. Eremtchenko, J.A. Schaefer, F.S. Tautz, Understanding and tuning the epitaxy of large aromatic adsorbates by molecular design, Nature 425 (2003) 602–605.
[18] M. Rohlfing, R. Temirov, F.S. Tautz, Adsorption structure and scanning tunneling data of a prototype organic-inorganic interface: PTCDA on Ag(111), Physical Review B 76 (2007) 115421.
[19] A. Kraft, R. Temirov, S.K.M. Henze, S. Soubatch, M. Rohlfing, F.S. Tautz, Lateral adsorption geometry and site-specific electronic structure of a large organic chemisorbate on a metal surface, Physical Review B 74 (2006) 041402.
[20] K. Glockler, C. Seidel, A. Soukopp, M. Sokolowski, E. Umbach, M. Bohringer, R. Berndt, W.D. Schneider, Highly ordered structures and submolecular scanning tunnelling microscopy contrast of PTCDA and DM-PBDCI monolayers on Ag(111) and Ag(110), Surface Science 405 (1998) 1–20.
[21] N. Nicoara, E. Roman, J.M. Gomez-Rodriguez, J.A. Martin-Gago, J. Mendez, Scanning tunneling and photoemission spectroscopies at the PTCDA/Au(111) interface, Organic Electronics 7 (2006) 287–294.
[22] F.S. Tautz, Structure and bonding of large aromatic molecules on noble metal surfaces: the example of PTCDA, Progress in Surface Science 82 (2007) 479–520.
[23] M. Rohlfing, R. Temirov, F.S. Tautz, Adsorption structure and scanning tunneling data of a prototype organic-inorganic interface: PTCDA on Ag(111), Physical Review B 76 (2007) 115421.
[24] C. Ludwig, B. Gompf, W. Glatz, J. Petersen, W. Eisenmenger, M. Mobus, U. Zimmermann, N. Karl, Video-Stm, Leed and X-Ray-Diffraction Investigations of Ptcda on Graphite, Zeitschrift Fur Physik B-Condensed Matter 86 (1992) 397–404.
[25] P. Fenter, F. Schreiber, L. Zhou, P. Eisenberger, S.R. Forrest, In situ studies of morphology, strain, and growth modes of a molecular organic thin film, Physical Review B 56 (1997) 3046–3053.
[26] B. Krause, A.C. Durr, K. Ritley, F. Schreiber, H. Dosch, D. Smilgies, Structure and growth morphology of an archetypal system for organic epitaxy: PTCDA on Ag(111), Physical Review B 66 (2002) 235404.
[27] A. Gerlach, S. Sellner, F. Schreiber, N. Koch, J. Zegenhagen, Substrate-dependent bonding distances of PTCDA: a comparative X-ray standing-wave study on Cu(111) and Ag(111), Physical Review B 75 (2007) 045401.
[28] A. Hauschild, K. Karki, B.C.C. Cowie, M. Rohlfing, F.S. Tautz, M. Sokolowski, Molecular distortions and chemical bonding of a large pi-conjugated molecule on a metal surface, Physical Review Letters 94 (2005) 036106.
[29] A. Hauschild, R. Temirov, S. Soubatch, O. Bauer, A. Scholl, B.C.C. Cowie, T.L. Lee, F.S. Tautz, M. Sokolowski, Normal-incidence x-ray standing-wave determination of the adsorption geometry of PTCDA on Ag(111): comparison of the ordered room-temperature and disordered low-temperature phases, Physical Review B 81 (2010) 125432.
[30] S.K.M. Henze, O. Bauer, T.L. Lee, M. Sokolowski, F.S. Tautz, Vertical bonding distances of PTCDA on Au(111) and Ag(111): relation to the bonding type, Surface Science 601 (2007) 1566–1573.
[31] P.A. Fenter, X-ray reflectivity as a probe of mineral-fluid interfaces: a user guide, Applications of Synchrotron Radiation in Low-Temperature Geochemistry and Environmental Sciences 49 (2002) 149–220.
[32] I.K. Robinson, D.J. Tweet, Surface X-ray-diffraction, Reports on Progress in Physics 55 (1992) 599–651.
[33] P. Fenter, Z. Zhang, Model-independent one-dimensional imaging of interfacial structures at <1 A resolution, Physical Review B 72 (2005) 081401.
[34] J.R. Fienup, Reconstruction of an object from modulus of its Fourier-transform, Optics Letters 3 (1978) 27–29.
[35] J. Hass, R. Feng, J.E. Millan-Otoya, X. Li, M. Sprinkle, P.N. First, W.A. de Heer, E.H. Conrad, C. Berger, Structural properties of the multilayer graphene/4H-SiC(000(1) overbar) system as determined by surface X-ray diffraction, Physical Review B 75 (2007) 214109.
[36] J. Hass, F. Varchon, J.E. Millan-Otoya, M. Sprinkle, N. Sharma, W.A. De Heer, C. Berger, P.N. First, L. Magaud, E.H. Conrad, Why multilayer graphene on 4H-SiC (000(1)over-bar) behaves like a single sheet of graphene, Physical Review Letters 100 (2008) 125504.
[37] J.A. Kellar, J.M.P. Alaboson, Q.H. Wang, M.C. Hersam, Identifying and characterizing epitaxial graphene domains on partially graphitized SiC(0001) surfaces using scanning probe microscopy, Applied Physics Letters 96 (2010) 143103.
[38] E.T. Foley, N.L. Yoder, N.P. Guisinger, M.C. Hersam, Cryogenic variable temperature ultrahigh vacuum scanning tunneling microscope for single molecule studies on silicon surfaces, The Review of Scientific Instruments 75 (2004) 5280–5287.
[39] A. Bauer, P. Reischauer, J. Krausslich, N. Schell, W. Matz, K. Goetz, Structure refinement of the silicon carbide polytypes 4H and 6H: unambiguous determination of the refinement parameters, Acta Crystallographica Section A 57 (2001) 60–67.
[40] P. Fenter, J.G. Catalano, C. Park, Z. Zhang, On the use of CCD area detectors for high-resolution specular X-ray reflectivity, Journal of Synchrotron Radiation 13 (2006) 293–303.
[41] M. Rauscher, H. Reichert, S. Engemann, H. Dosch, Local density profiles in thin films and multilayers from diffuse X-ray and neutron scattering, Physical Review B 72 (2005) 205401.
[42] J. Miao, J. Kirz, D. Sayre, The oversampling phasing method, Acta Crystallographica. Section D: Biological Crystallography 56 (2000) 1312–1315.
[43] R. Feidenhansl, Surface-structure determination by X-ray-diffraction, Surface Science Reports 10 (1989) 105–188.
[44] H. Huang, S. Chen, X.Y. Gao, W. Chen, A.T.S. Wee, Structural and electronic properties of PTCDA thin films on epitaxial graphene, ACS Nano 3 (2009) 3431–3436.
[45] J. Als-Nielsen, D. McMorrow, Elements of Modern X-ray Physics, John Wiley & Sons Ltd, West Sussex, 2000.
[46] WarrenB.E. , X-ray Diffraction, 3rd edCourier Dover Publications, New York, 1990.
[47] Y. Yoneda, Anomalous surface reflection of X-rays, Physical Review 131 (1963) 2010.
[48] Here, $\chi^2 = (_k(I_k - I_{calc,k})^2/\sigma_k^2)/(N-N_p)^2$, where I_k and $I_{calc,k}$ are the measured and calculated intensities for the kth data point, respectively, σ_k is the corresponding uncertainty for the data point, and N and N_p are the number of data points and fitting parameters, respectively. Similarly, R-factor $= _k|(I_k - I_{calc,k})^2/I_k|/N$.
[49] C. Riedl, U. Starke, Structural and electronic properties of epitaxial graphene on SiC (0001), Silicon Carbide and Related Materials 2008 (615–617) (2009) 219–222.
[50] C. Riedl, U. Starke, J. Bernhardt, M. Franke, K. Heinz, Structural properties of the graphene-SiC(0001) interface as a key for the preparation of homogeneous large-terrace graphene surfaces, Physical Review B 76 (2007) 245406.
[51] G.M. Rutter, J.N. Crain, N.P. Guisinger, T. Li, P.N. First, J.A. Stroscio, Scattering and interference in epitaxial graphene, Science 317 (2007) 219–222.
[52] F. Varchon, P. Mallet, J.Y. Veuillen, L. Magaud, Ripples in epitaxial graphene on the Si-terminated SiC(0001) surface, Physical Review B 77 (2008) 235412.
[53] See online Supporting Information.
[54] T. Ohta, N.C. Bartelt, S. Nie, K. Thürmer, G.L. Kellogg, Role of carbon surface diffusion on the growth of epitaxial graphene on SiC, Physical Review B 81 (2010) 121411.
[55] M. Hupalo, E.H. Conrad, M.C. Tringides, Growth mechanism for epitaxial graphene on vicinal 6H-SiC (0001) surfaces: a scanning tunneling microscopy study, Physical Review B 80 (2009) 041401.

[56] V. Borovikov, A. Zangwill, Step bunching of vicinal 6H-SiC 0001 surfaces, Physical Review B 79 (2009) 245413.
[57] S. Nakamura, T. Kimoto, H. Matsunami, S. Tanaka, N. Teraguchi, A. Suzuki, Formation of periodic steps with a unit-cell height on 6H-SiC (0001) surface by HCl etching, Applied Physics Letters 76 (2000) 3412–3414.
[58] L.I. Johansson, F. Owman, P. Mårtensson, High-resolution core-level study of 6H-SiC(0001), Physical Review B 53 (1996) 13793.
[59] T. Seyller, K.V. Emtsev, K. Gao, F. Speck, L. Ley, A. Tadich, L. Broekman, J.D. Riley, R.C.G. Leckey, O. Rader, A. Varykhalov, A.M. Shikin, Structural and electronic properties of graphite layers grown on SiC(0001), Surface Science 600 (2006) 3906–3911.
[60] A. Gerlach, S. Sellner, S. Kowarik, F. Schreiber, In-situ X-ray scattering studies of OFET interfaces, Physica Status Solidi A Applications and Material Science 205 (2008) 461–474.
[61] A. Bondi, Van der Waals volumes and radii, The Journal of Physical Chemistry 68 (1964) 441–451.
[62] X.Q. Tian, J.B. Xu, X.M. Wang, Self-Assembly of PTCDA Ultrathin Films on Graphene: Structural Phase Transition and Charge Transfer Saturation, The Journal of Physical Chemistry C, (2010), doi:10.1021/jp1031674.
[63] M. Toerker, T. Fritz, H. Proehl, F. Sellam, K. Leo, Tunneling spectroscopy study of 3, 4, 9, 10-perylenetetracarboxylic dianhydride on Au(100), Surface Science 491 (2001) 255–264.